

A Balance of Unimolecular and Bimolecular Pathways Control the Temperature-Dependent Kinetics of Ozonolysis in Aerosols

Ryan S. Reynolds,^{1,2} and Kevin R. Wilson^{1,*}

¹*Chemical Sciences Division, Lawrence Berkeley National Laboratory, Berkeley, CA, 94720, USA*

²*Department of Chemistry, University of California, Berkeley, CA 94720, USA*

Abstract:

To better understand the key kinetic mechanisms controlling heterogeneous oxidation in organic aerosols, submicron particles composed of an alkene and a saturated carboxylic acid are exposed to ozone in a variable-temperature flow tube reactor. Effective uptake coefficients (γ_{eff}) are obtained from the multiphase reaction kinetics, which are quantified by Vacuum Ultraviolet Photoionization Aerosol Mass Spectrometry. For aerosols composed of only of alkenes, γ_{eff} doubles (from 6×10^{-4} to 1.2×10^{-3}) when the temperature is decreased from 293 to 263 K. Alternatively, for an alkene particle doped with a carboxylic acid, an efficient scavenger of stabilized Criegee Intermediates (sCI), γ_{eff} is observed to be weakly temperature dependent. A kinetic model, benchmarked to literature data, explains these results as arising from the temperature dependent competition between unimolecular pathways of sCI that promote radical chain cycling and those bimolecular pathways that form stable chain termination products (*i.e.*, α -acyloxyalkyl hydroperoxides). The implication of these results for the kinetics of aerosol aging at low temperatures is discussed.

* Correspondence to: krwilson@lbl.gov

Introduction

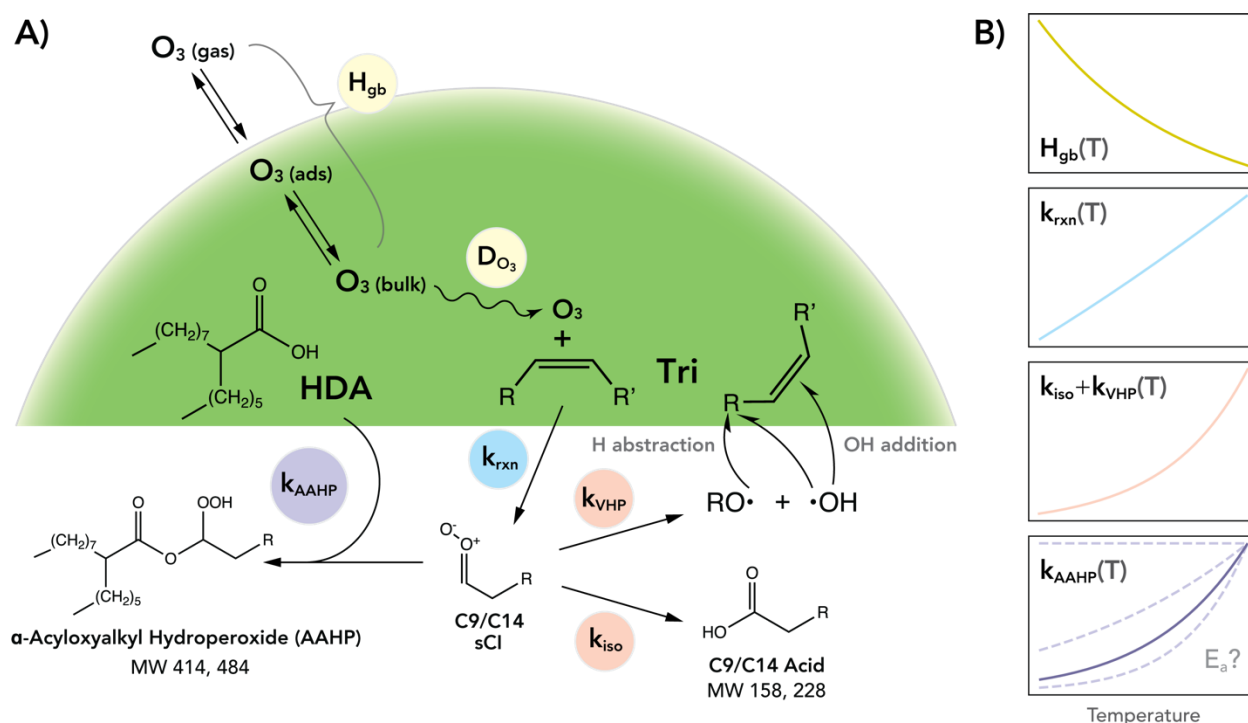


Figure 1. (A) Illustrated mechanism of the key chemical reactions considered in this study. (B) Depictions of the temperature dependence of the most important parameters controlling the heterogeneous reaction kinetics in this study.

Reactions between trace gases and aerosol particles are controlled by multiple physical and chemical processes, as illustrated in Figure 1A. These include adsorption and desorption of the trace gas from the particle surface, the transfer of the trace gas from the surface into the particle bulk and the reaction rate of the trace gas with particle-phase reactants.^{1–3} The rates of each of these individual steps depend on the identity of the trace gas and the chemical composition of the particle, as well as its physical properties such as viscosity and phase state.^{4–7} The coupling of these system-dependent transport and reaction processes can make predictions of chemical kinetics in these systems difficult and computationally intensive, especially when the reaction mechanism

in the particle phase is complex.^{8,9} In particular, reactions involving organic molecules, such as the ozonolysis of alkenes, can initiate a wide variety of secondary reaction steps and reaction products, driven by short-lived reactive intermediates embedded in complex reaction networks.^{10–13} Thus, it is desirable to find a way of disentangling these various processes in order to understand how these complex kinetics dynamically evolve during the course of reaction.

While many measurements of heterogeneous kinetics in aerosols have been conducted at a single ambient temperature, the number of variable-temperature measurements has grown in recent years.^{7,14,15} These studies are often motivated by an effort to better understand aging kinetics of organic aerosol in cold regions of the atmosphere, such as in the arctic, where organic aerosols constitute up to 40% of observed particulate mass.^{16,17} However, the key parameters controlling the heterogeneous reactivity often have differing responses to temperature, as illustrated in Figure 1B. For example, while gas solubility in liquids, described by the Henry's law constant between gas and bulk phases, H_{gb} in Fig. 1, tends to increase with decreasing temperature,^{18–20} the primary ozonolysis step, described by the rate constant (k_{rxn} , Fig. 1) is expected to exhibit a positive temperature dependence due to the activation energy for the reaction.²¹ Additionally, unimolecular chemical reactions of the stabilized Criegee Intermediates (hereafter referred to as sCI) generated by ozonolysis, such as isomerization to form carboxylic acids (k_{iso} , Fig. 1B) or decomposition into an alkoxy and an OH radical (k_{VHP} , Fig. 1B), have rates that depend strongly on both temperature and the molecular structure of the intermediate.^{22–25} Although there are many experimental or theoretical estimates for the temperature dependence of many of the rate constants in the gas-phase listed above, there is a need for more precise kinetic measurements in the particle phase as emphasized in recent work.^{8,26} In particular, the reaction rate constant for sCI and carboxylic acids in the particle phase, denoted here by k_{AAHP} , has been shown to be significantly slower in the

particle phase than in the gas phase.^{27–29} This result could be an indication of an energetic barrier to reaction in the condensed phase, in contrast to the barrierless mechanism in the gas phase.^{28,29} Temperature-dependent measurements of this rate can aid in uncovering the mechanism of this reaction, as well as inform estimates of the branching ratio between bimolecular and unimolecular reactions of the sCI, which is key to understanding ozonolysis kinetics in model aerosols.

To better understand these facets of heterogeneous reactions in the particle phase, this study builds on previous work by examining the ozonolysis kinetics of organic aerosols composed of binary mixtures of *cis*-9-Tricosene (**Tri**, C₂₃H₄₆) and 2-hexyldecanoic acid (**HDA**, C₁₆H₃₂O₂) as a function of temperature (253 to 293 K). This study aims to quantify the contributions of the competing processes outlined above to the total reactivity in this heterogeneous reaction, and to identify the relative importance of reactant transport and primary and secondary chemical reactions to the temperature-dependent behavior of the reactive uptake of ozone. To this end, a detailed reaction-diffusion model is developed to compare with the experimental results, first for the pure alkene aerosol to probe the effects of temperature on the network of secondary reactions initiated by ozonolysis, and second in the presence of varying amounts of HDA, to probe the temperature-dependent branching ratio between bimolecular and unimolecular sinks of particle-bound sCI. Where necessary, estimates are made of thermodynamic parameters, such as the activation energy (E_a) for the reaction of sCI with a carboxylic acid (**k_{AAHP}**), with the parameter choice evaluated against experimental results. Together, experimental and modeling results reveal how the observed kinetics are the result of competitions between unimolecular and bimolecular reaction steps, which are in a delicate balance across the temperature range studied here. These results highlight the crucial role that reactive intermediates can play in aerosol aging at low temperatures.

Methods

Experimental Setup

The experimental setup is modified slightly from that described in previous work and is diagrammed in detail in Figure S1 (Supporting Information). Briefly, a jacketed quartz flow tube reactor is used to measure the ozonolysis kinetics on aerosols composed of binary mixtures of Tri and HDA. The temperature of the flow tube is controlled by a recirculating chiller (VWR, AD15R), which flows a mixture of equal parts water and ethylene glycol (Macron Fine Chemicals) through the outer jacket of the flow tube. Experiments are conducted at temperatures in 10 degree intervals from 253 K to 293 K as measured by the chiller's internal thermostat. The reactor temperature is allowed to equilibrate to within $\pm 1^\circ\text{C}$ of the nominal temperature before each experiment.

Particles are generated *via* homogeneous nucleation by passing 0.3 SLM room temperature ($\sim 20^\circ\text{C}$) dry nitrogen through heated organic vapor in a Pyrex tube inserted into an annular furnace (Carbolite) held at 115–120 $^\circ\text{C}$. A narrow particle size is then selected from the resulting polydisperse particle distribution using an Aerodynamic Aerosol Classifier (AAC, Cambustion Instruments) set to 370 nm diameter, with a sheath flow of 3 LPM. To allow the particle-laden flow additional time to equilibrate to the temperature, the flow is passed through a length of $\frac{1}{2}$ in. copper tubing submerged in the bath of the chiller prior to entering the flow tube. The particle size distribution is measured at the exit of the flow tube before and after reaction using a Scanning Mobility Particle Spectrometer (SMPS) comprised of a condensation particle counter (CPC 3025A, TSI Inc.) and a differential mobility analyzer (DMA 3071, TSI Inc.).

Mass Spectrometry

Mass spectra were recorded using Vacuum Ultraviolet (VUV) photoionization Aerosol Mass Spectrometer (VUV-AMS) endstation at the Chemical Dynamics Beamline (9.0.2) at the Advanced Light Source, Berkeley, CA. The instrument has been described in detail previously,³⁰

and a schematic overview is available in the supporting information (Figure S2). Spectra were obtained at photon energies between 9.8–10.2 eV, above the photoionization threshold for both Tri and HDA. Aerosols sampled by the AMS were flash vaporized at a temperature of 145–155 °C before photoionization, and each spectrum collected is the average of at least 10,000 detector sweeps. The mass spectrum of the unreacted aerosol is shown in Figure 2. Photoionization of Tri primarily produces a molecular ion at $m/z = 322$, as well as a series of lower-intensity peaks corresponding to fragments produced by alkyl loss. Photoionization of HDA at the same photon energy yields a molecular ion at $m/z = 256$, however the branched structure of HDA facilitates further fragmentation at the carbon adjacent to its carboxylic acid head group. The resulting fragments correspond to loss either of the hexyl group, yielding a 10-carbon fragment with $m/z = 172$, or the octyl group, resulting in an 8-carbon fragment at $m/z = 144$. Reaction kinetics are monitored as a function of ozone exposure by varying the ozone concentration in the flow tube and recording the changes in integrated intensity of the reactant and product peaks from the VUV-AMS.

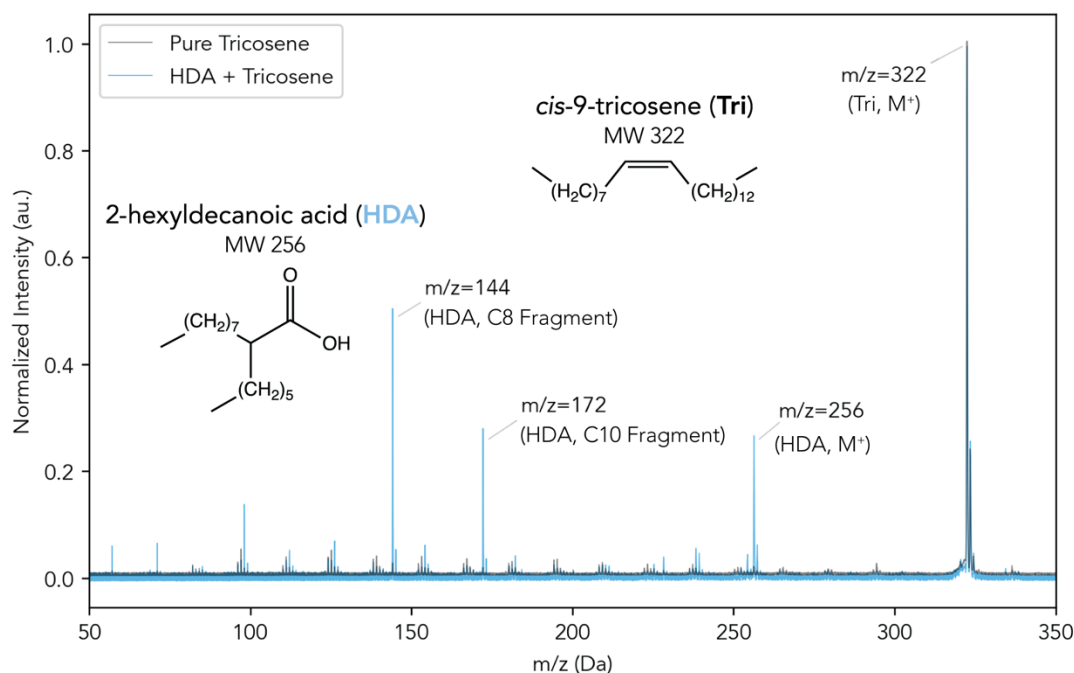


Figure 2. VUV Photoionization spectrum of pure Tri aerosols (black spectrum) or mixed HDA and Tri aerosols (blue spectrum) before ozone exposure. Intensities are normalized to the molecular ion of Tri ($m/z = 322$), apparent in both spectra. Labeled peaks in the blue spectrum ($m/z = 256$, 172, and 144) are identified as unique to HDA, with peak assignments described in the text.

Kinetic Model Description

Due to the complexity of the coupled chemical reaction and transport network described in Figure 1A, a reaction-diffusion model was developed to simulate the expected temperature-dependent heterogeneous kinetics of the ozonolysis reaction in this system. This is done using Kinetiscope (<https://hinsberg.net/kinetiscope/>), a stochastic reaction-diffusion simulator.³¹ Previously, Kinetiscope has been used to model this reaction at room temperature using a single, well-mixed compartment description.^{29,32} In order to properly model the temperature dependence of the chemical transport processes, the previous framework has been adapted to a two-

compartment description with explicit surface and bulk regions connected by diffusion pathways, similar to the framework described by Willis and Wilson.⁹

Following the approach of previous work modeling aqueous droplets,^{3,9} the adsorption, desorption and solvation kinetics of ozone at the gas-particle interface are determined according to a coupled-equilibrium model, with the equilibrium constants (*e.g.*, H_{gb}) constrained by experimental measurements and the results of Molecular Dynamics (MD) simulations, as described in the *Supporting Information*. Rate constants for chemical reaction steps are assumed to have Arrhenius-like temperature dependence, with parameters taken from experimental measurements (or those of the analogous gas-phase reactions) given in literature. In the case of the primary ozonolysis rate (k_{rxn}), a solution-phase measurement is used to determine the magnitude of the reaction rate constant at room temperature, while the activation energy is chosen within a range constrained by tabulated gas phase data, as described in the *Supporting Information*. The activation energy (E_a) for k_{AAHP} is a key parameter in need of constraint; in this study, several possible values of E_a are chosen and evaluated for their agreement with the experimental data describing the decay of HDA, as discussed in subsequent sections. The complete reaction mechanism employed in the final simulations, including the Arrhenius parameters describing the rate constant for each step, is given in Table S1 (*Supporting Information*).

Results

Tri Decay Kinetics

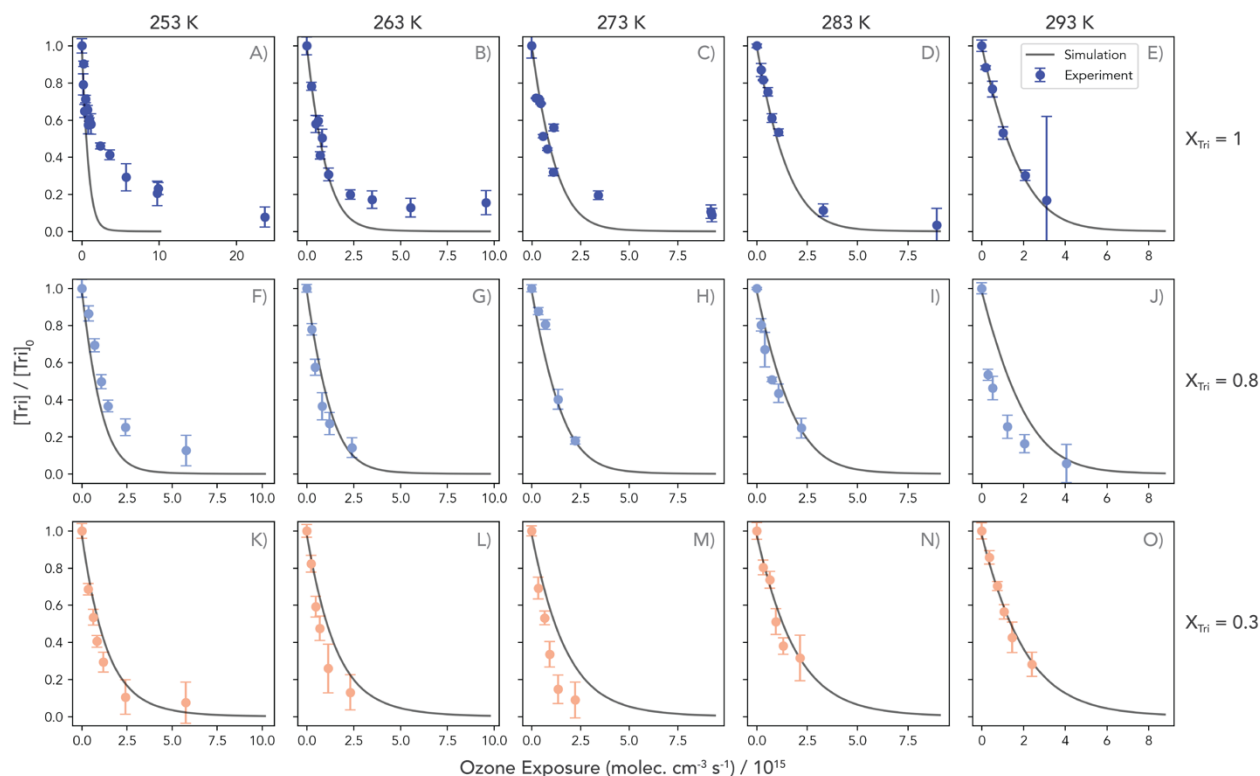


Figure 3. Decay kinetics of Tri ($m/z = 322$) from VUV-AMS experiments and kinetic simulations across all experimental conditions of this study, normalized to initial Tri signal intensity (experiments, points) or concentration (simulations, lines). Initial mole fractions of Tri (X_{Tri}) are constant across rows, as labeled at the right hand side of the figure: $X_{\text{Tri}}=1$ (panels A–E), $X_{\text{Tri}}=0.8$ (F–J), and $X_{\text{Tri}}=0.3$ (K–O). Data points are colored according to initial X_{Tri} for additional emphasis. Columns denote constant temperatures, as labeled at the top of the figure. Error bars on points correspond to relative (percent) error of ± 1 standard deviation from the mean of the signal intensity measured by the VUV-AMS.

The normalized decay kinetics of Tri vs. ozone exposure (i.e. $[\text{O}_3] \times \text{time}$) are shown in Figure 3. As seen from the changing scale of the ozone exposure axis, the rate of decay of Tri generally increases with decreasing temperature (proceeding right to left along a row), and with increasing initial X_{Tri} (proceeding from the top to the bottom panel). Lines represent the output of kinetic simulations.

For pure Tri aerosols (panels A-E in Figure 3), an initial region of decay is apparent at small ozone exposures and generally in agreement with the simulated kinetics, with several exceptions. A fraction of Tri remaining unreacted begins to be apparent below 273 K (panels A-C), and at 253 K (panel A), and a distinct shift towards slower decay kinetics can be observed at large exposures. This change in kinetics is taken as an indication of the onset of a phase transition in the aerosols that is induced during the course of reaction. Since the freezing point of Tri has been reported as -0.6 °C (272.5 K) by FTIR measurements, the onset of this apparent phase change below 263 K does not directly correspond to the bulk freezing transition.³³ However, supercooling of organic aerosols by more than 30 °C below the bulk freezing points of their constituents has been observed in other studies where particles are produced *via* homogeneous nucleation.^{34,35,7} As such, it seems likely that the biexponential behavior observed in panel A is the onset of a phase transition, and, by extension, that the kinetics observed at 263 K and above (panels B-E) correspond to supercooled liquid particles. Similarly, as the bulk freezing temperature of HDA is reported to be 18 °C (291 K),³⁶ the onset of bi-exponential kinetics in panel F, where $X_{\text{Tri}}=0.8$, could also correspond to the onset of freezing of supercooled aerosol particles, accounting for the discrepancy between simulation and experiment at 253 K. Similar behavior was observed by Katrib *et al.* for room temperature ozonolysis of mixed oleic and stearic acid particles, and was attributed to the complex phase behavior of the mixture of the two lipids.³⁵ Composition- and temperature-dependent phase behavior, such as differing particle morphologies forming at low temperatures due to the interaction of the aerosol components, could be responsible for the discrepancy between the trends in kinetics for $X_{\text{Tri}}=0.8$ and $X_{\text{Tri}}=0.3$.

Effective Uptake Coefficients (γ_{eff}) vs. Temperature

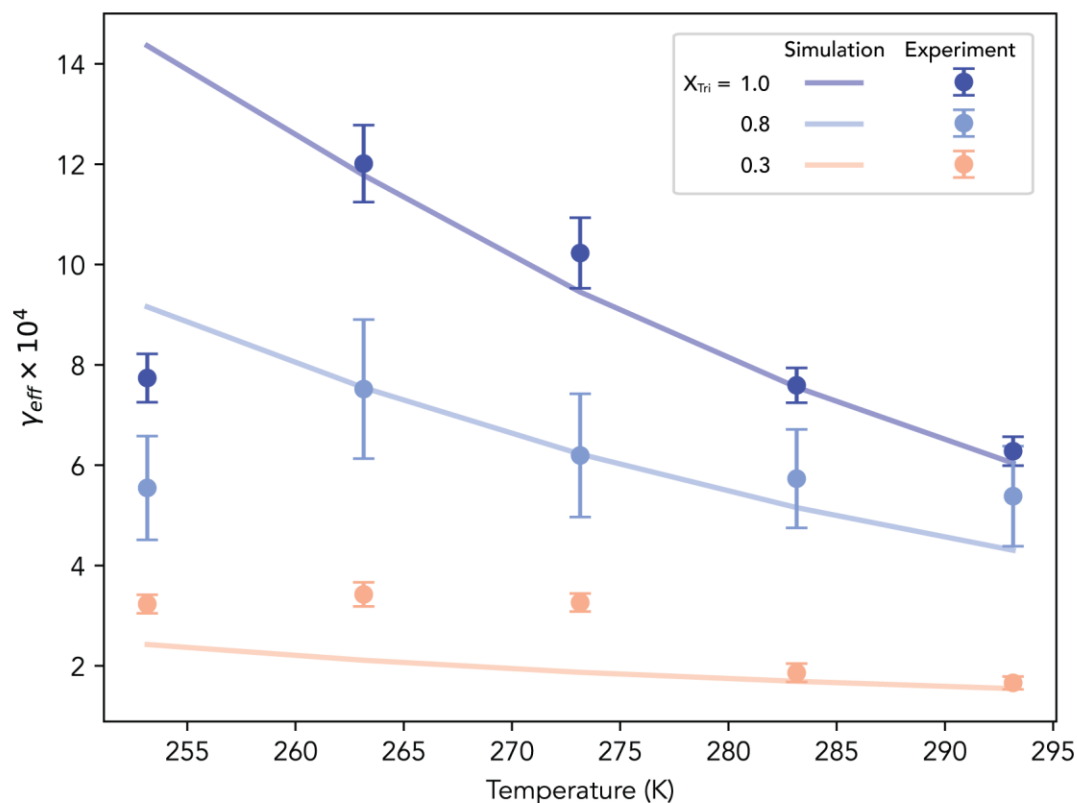


Figure 4. Effective uptake coefficients (γ_{eff}) of Tri calculated from experiment (points) and simulation (lines) as a function of temperature. Initial X_{Tri} is denoted by color, decreasing top to bottom, from $X_{Tri}=1$ to $X_{Tri}=0.3$. Error bars on points correspond to Tri decay constant fits assuming ± 1 standard deviation from the mean.

In order to evaluate the kinetics of Tri decay quantitatively across experimental conditions, the effective uptake coefficient (γ_{eff}) was calculated for each experiment,

$$\gamma_{eff} = \frac{4 \cdot D_p [Tri]_0 k_{obs}}{6\bar{c}} \cdot X_{Tri} \quad (1)$$

where D_p is the particle diameter in cm, $[Tri]_0$ is the number density of liquid Tri in molec. cm⁻³. X_{Tri} is the initial mole fraction of Tri in the aerosol, and \bar{c} is the mean speed of ozone in cm s⁻¹. The initial region of each Tri decay curve in Figure 3 was fit by an exponential function, from

which the decay constant k_{obs} (in $\text{cm}^3 \text{ molec.}^{-1} \text{ s}^{-1}$) is obtained from each experiment. The resulting trends in γ_{eff} for each experimental condition are shown in Figure 4.

As discussed previously,^{29,32} γ_{eff} differs from a traditional uptake coefficient measured *via* the consumption of a gas-phase reactant as it includes all reactions that consume the condensed-phase reactant, including secondary radical reactions. Zeng *et al.* found that the γ_{eff} was 6×10^{-4} for ozonolysis of polydisperse Tri aerosols at 298 K,³² consistent with the values at 293 K reported here.²⁹ This is roughly an order of magnitude higher than the traditional uptake coefficient of O_3 on Tri measured by Wells,³⁷ and the discrepancy between these values is evidence that radical secondary chemistry is involved in the underlying mechanism.

The trends in γ_{eff} vs. temperature and X_{Tri} , shown in Figure 4, exhibit interesting behavior: for pure Tri aerosol (dark blue points, Figure 4), γ_{eff} increases monotonically by roughly a factor of 2 as temperature decreases from 293 to 263 K. As discussed in the previous section, the experiment then shows a marked drop from 263 to 253 K not predicted by simulations, attributed to changes in particle phase. As the initial HDA concentration is increased in Figure 4 ($X_{\text{Tri}}=0.8$, light blue points; and $X_{\text{Tri}}=0.3$, light orange points), γ_{eff} decreases. At 293 K, the uptake falls to 5×10^{-4} and 2×10^{-4} for aerosols with $X_{\text{Tri}}=0.8$ and 0.3, respectively, consistent with previous measurements of these kinetics *via* APCI-MS.²⁹ The trend with X_{Tri} generally holds as temperature decreases, however the slope of γ_{eff} with temperature is less steep at high HDA concentrations. The trend for $X_{\text{Tri}}=0.8$ ($X_{\text{HDA}}=0.2$) looks nearly identical to that for pure Tri aerosol, with γ_{eff} nearly doubling from 293 to 263 K, followed by a drop at 253 K, attributed to the onset of particle freezing. Finally, when HDA is 70% of the initial aerosol composition ($X_{\text{Tri}}=0.3$), values of γ_{eff} plateau at 3×10^{-4} at 273 K, exhibiting no sharp decrease at the lowest temperature.

HDA Decay Kinetics

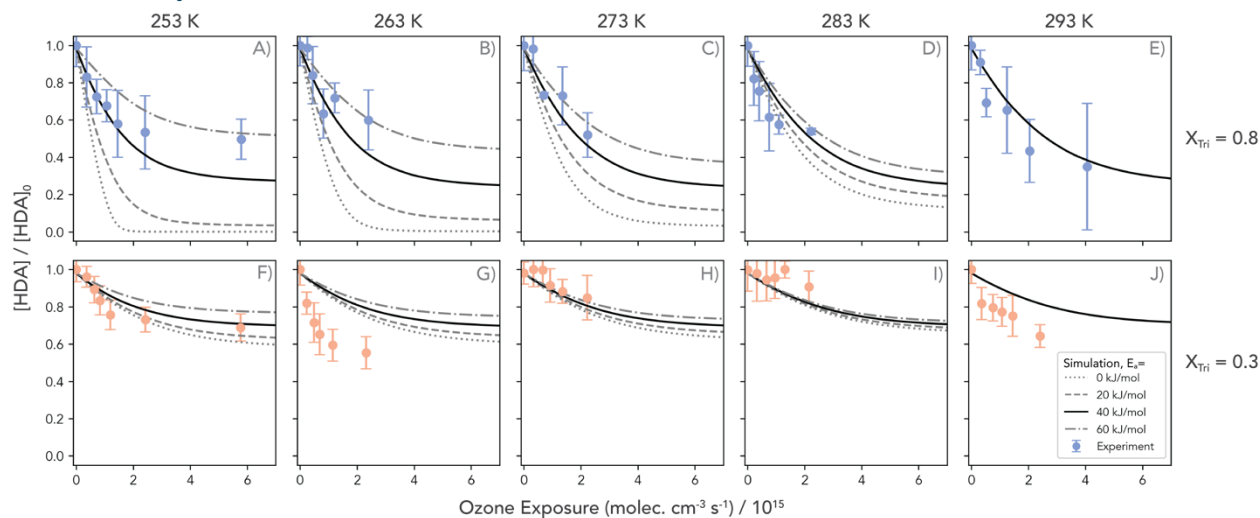


Figure 5. HDA decay kinetics from the $m/z = 256$ peak (points) normalized to the initial signal intensity, with simulation results overlaid (lines). Simulations assume four different temperature dependent descriptions of k_{AAHP} corresponding to activation energies (E_a) of 0, 20, 40, and 60 kJ mol^{-1} (denoted by line style).

The decay kinetics of HDA are monitored *via* the decay in intensity of the molecular ion peak at $m/z = 256$, as shown in Figure 5. As described previously, HDA fragment ions are observed at $m/z = 172$ and 144, and exhibit nearly identical kinetics to the molecular ion peak (see Figures S8 and S9, *Supporting Information*). Consistent with previous observations,²⁹ the fraction of the initial HDA remaining at long ozone exposures reaches a non-zero limiting value that depends on the initial composition of the aerosol: a larger fraction of the HDA is consumed when a smaller amount of HDA is initially present in the particle. The decay of HDA is attributed to the reaction the carboxylic acid functionality with the sCI, which can also be consumed in competing unimolecular reactions (Fig. 1). As such, the decay kinetics of HDA can serve as a probe of the branching ratio between these pathways. Notably, the limiting fraction of HDA remaining does not seem to change dramatically across temperatures, suggesting that the change to the branching ratio over this temperature range may be small.

As discussed in more detail later, the temperature-dependent unimolecular decay reaction rate constants of the sCI produced in this mechanism have been constrained by gas phase measurements and theoretical estimates,²² leaving the temperature dependence of the bimolecular rate constant, k_{AAHP} , free to be optimized to reproduce the experimental results. This rate constant has been found to have no activation barrier for small sCI reacting with small acids in the gas phase,²⁸ but previous work indicates that the particle phase reaction proceeds at a rate much slower than the expected liquid phase diffusion limit. Kinetic modeling is used to explore the behavior of this reaction mechanism assuming several different values for the activation energy (E_a) to assess a reasonable range of values for this parameter given the HDA decay kinetics observed in these experiments.

Optimization of $k_{AAHP}(T)$

The temperature dependence of k_{AAHP} is described using the Arrhenius equation,

$$k_{AAHP} = A \cdot e^{\frac{-E_a}{RT}} \quad (2)$$

where A is the pre-factor, with the same units as the rate constant ($\text{cm}^3 \text{ molec.}^{-1} \text{ s}^{-1}$), and E_a is the activation energy barrier in kJ mol^{-1} . As seen in Figure 5, simulations were carried out assuming four different E_a (0, 20, 40, and 60 kJ mol^{-1}). Pre-factors are calculated for each activation energy by assuming no temperature dependence in the pre-factor and by fixing the rate constant at 293 K to be equal to $2.1 \times 10^{-19} \text{ cm}^3 \text{ molec.}^{-1} \text{ s}^{-1}$, which is within one standard deviation of the value from previous measurements ($1.85 \pm 0.27 \times 10^{-19} \text{ cm}^3 \text{ molec.}^{-1} \text{ s}^{-1}$) and in accordance with the optimal value of k_{AAHP} previously used in previous simulations.²⁹ Values of the pre-factor corresponding to each choice of E_a are reported in Table S2, and plots of the corresponding behavior of k_{AAHP}

with temperature for each set of Arrhenius parameters is shown in Figure S10 (*Supporting Information*).

In the top row of Figure 5, simulation results for each activation energy are overlaid on the experimental data for the decay of HDA observed during ozonolysis of particles with $X_{\text{Tri}}=0.8$. At 293 K (panel E), all of the simulation lines lie atop one another by construction, but as temperature decreases (moving to the left, toward panel A), the model predictions for the extent of the HDA decay diverge. Smaller activation energies (0, 20 kJ mol⁻¹) lead to more extensive HDA decay, while the largest activation energies (40 and 60 kJ mol⁻¹) result in small to moderate decreases in HDA.

The temperature-dependent trend in the experimental data for $X_{\text{Tri}}=0.8$ is modest, with little change in the extent of HDA decay predicted as temperature decreases, and agreement is good between experiments and simulations with an E_a of at least 40 kJ mol⁻¹. This value aligns with predictions for the minimal change in HDA decay kinetics over this temperature range from the analytical expression for HDA decay kinetics derived in previous work.²⁹ (Figure S11, *Supporting Information*) The simulation results corresponding to an E_a of 40 kJ mol⁻¹ have been bolded in Figure 5. For the data where $X_{\text{Tri}}=0.3$, the model and experiments agree sufficiently between 273 and 293 K, with model predictions for nearly all activation energies lying within the experimental error. Agreement is poorer at lower temperatures, where phase effects due to the higher freezing point of HDA may interfere with reaction at the lowest temperatures, as discussed previously.

Reaction Products

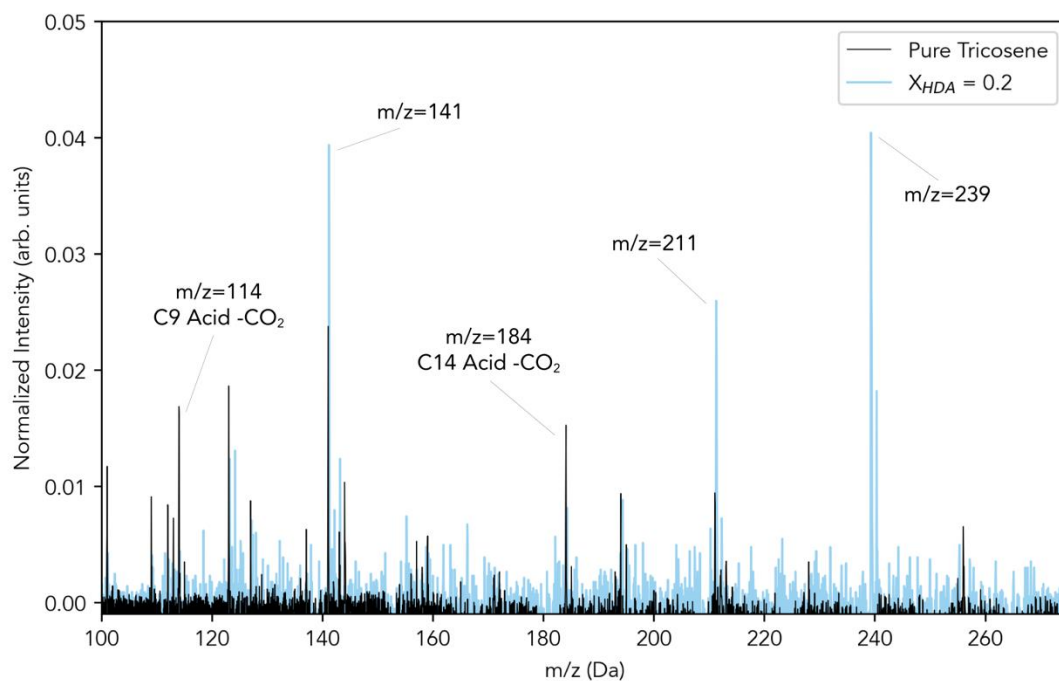


Figure 6. Difference Mass spectrum of products from ozonolysis of pure Tri aerosol (black spectrum) and an aerosol mixture with $X_{\text{Tri}}=0.8$, $X_{\text{HDA}}=0.2$ (blue spectrum) at 263 K.

Unimolecular sCI Reaction Products

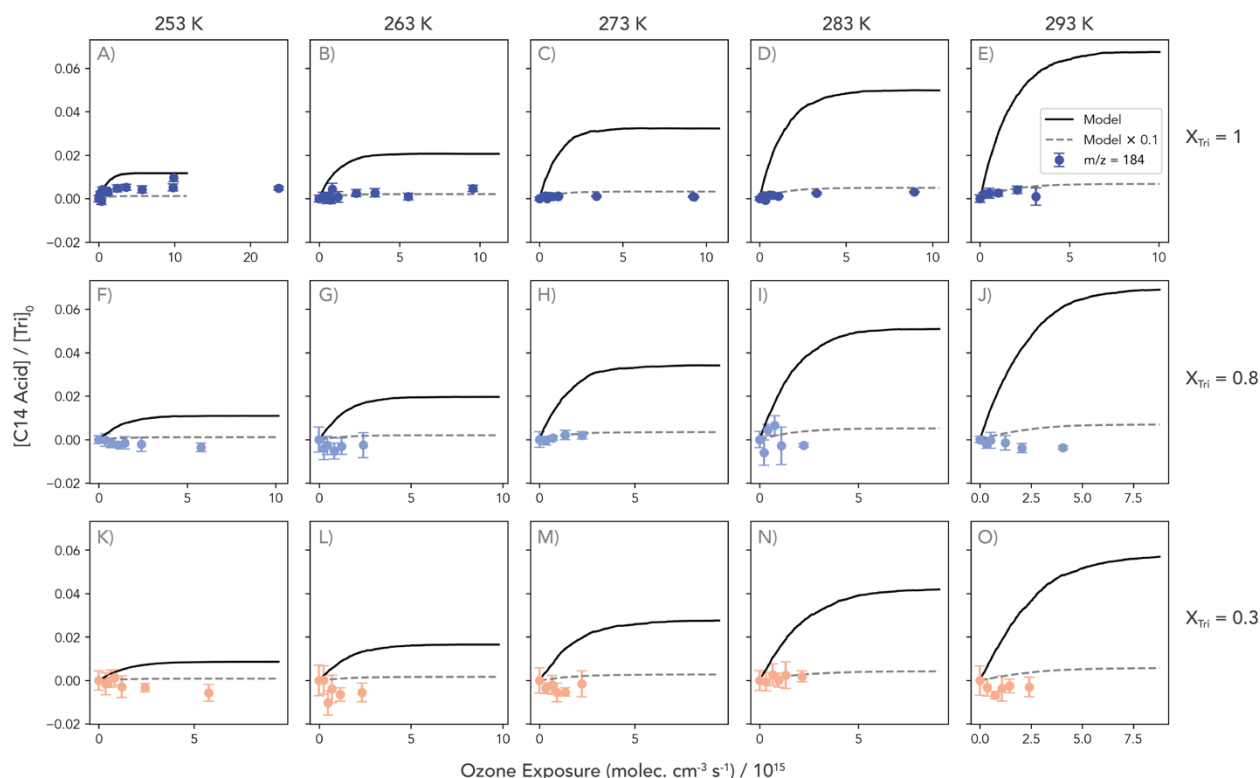


Figure 7. Observed kinetics of $m/z=184$ peak from AMS experiments and C14 acid kinetics from simulations across all conditions represented in this study, normalized to initial Tri signal intensity (experiments, points) or concentration (simulations, lines), respectively. The simulation results scaled down by a factor of 10 have also been overlaid for comparison.

As seen in the difference mass spectrum shown in Figure 6, a complex landscape of fragments of reaction products formed from Tri ozonolysis are visible. Two peaks of note are found at $m/z = 114$ and 184, which are identified as the decarboxylation ($M-CO_2$) fragments of the carboxylic acids formed by isomerization of the C9 and C14 sCI (nonanoic acid, MW 158, and tetradecanoic acid, MW 228 — see Figure 1A). The growth kinetics of $m/z = 184$ normalized to the initial Tri intensity are displayed in Figure 7, showing that these decarboxylation fragments, corresponding to sCI isomerization, only have apparent kinetics in case of pure Tri, where no HDA is present. Corresponding product kinetics and model predictions for $m/z = 114$, corresponding to

the decarboxylation fragment of nonanoic acid, are nearly identical and are shown in Figure S5 (*Supporting Information*). For aerosols with $X_{\text{Tri}}=0.8$ or 0.3, these peaks show zero or negative growth relative to the background. Since the small acids assigned to these peaks are formed exclusively by isomerization of the sCI, the lack of growth kinetics for these isomerization products in the presence of HDA suggests that the reaction between sCI and HDA outcompetes this isomerization pathway at all temperatures. Instances of negative kinetics are likely due to fragments produced by ionization of unreacted Tri, which are isobaric with the assigned decarboxylation fragments, thus decreasing below their background intensities as the reaction proceeds and Tri is consumed.

Simulation Results

The temperature-dependent rate of the sCI isomerization step, k_{iso} , defined in the model is taken from the theoretical structure-activity relationship (SAR) of Vereecken *et al.*,²² for a primary ethyl sCI in its *anti*-conformer (with the O-O bond facing away from the alkyl chain). The sCI undergoes a 1,3-cyclization reaction to form a dioxirane intermediate, followed by a ring-opening and hydrogen shift to form a carboxylic acid. The rate of this unimolecular process is on the order of 70 s^{-1} at 293 K and decreases by nearly two orders of magnitude as the temperature approaches 253 K, resulting in the trend evident in the simulation results in Figure 7: a decrease in the predicted yield of the isomerization product with decreasing temperature. Scaling the simulated predictions down by an order of magnitude allows for reasonable agreement with the experimental data when $X_{\text{Tri}}=1$, but the experimental data does not exhibit the expected trend in product yield with temperature. A combination of factors could contribute to this discrepancy, including a *syn:anti* sCI conformer ratio produced by Tri ozonolysis that favors *syn* conformers, in contrast to the 1:1 ratio assumed here for simplicity.^{38,39} Additionally, the temperature-dependent trend could be

obscured by the scavenging of the isomerization product acids by subsequent reaction with an sCI, as discussed in the following section. However, the disappearance of these isomerization products in the presence of HDA still provides a benchmark for the magnitude of this unimolecular sink for the particle-phase sCI, namely that it is smaller than the sCI + HDA sink under these conditions.

Bimolecular sCI Reaction Products

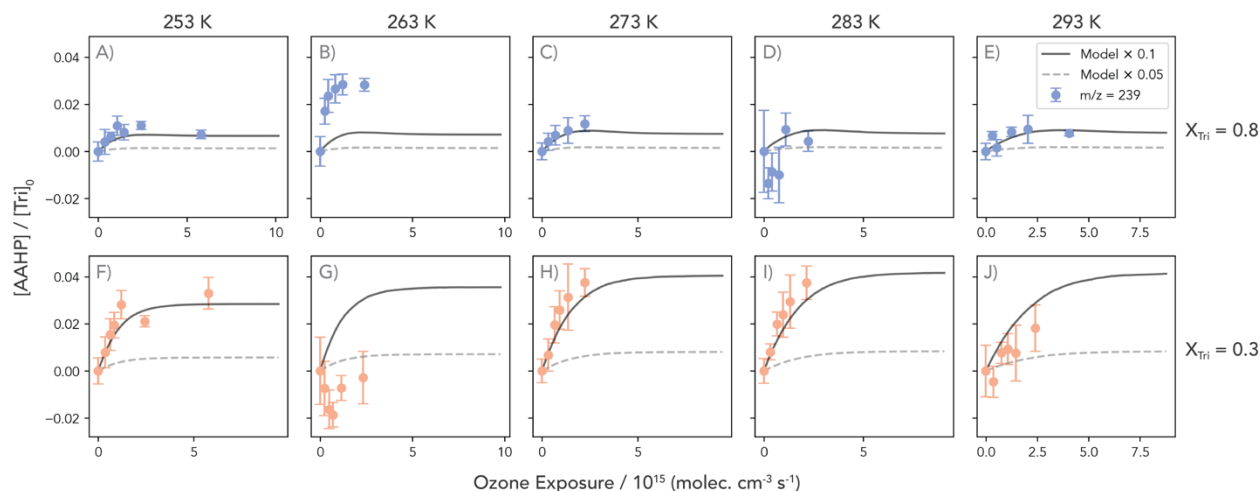


Figure 8. Observed kinetics of the $m/z = 239$ peak, identified as the C-O cleavage fragment of the HDA-derived AAHPs (see Scheme S1). Signal intensities are normalized to the initial intensity of the Tri peak ($m/z = 322$) for each experimental condition. The predicted kinetics of the total AAHP production relative to initial Tri concentration ($[Tri]_0$) from the explicit kinetic simulations, scaled down by a factor of 10 and by factor of 20, have been overlaid for comparison.

In the difference spectrum for mixed Tri/HDA aerosols shown in Figure 6 (light blue spectrum), the three most prominent peaks are all of odd-integer mass, suggesting fragmentation from a larger molecule: $m/z = 239$ is observed as a product exclusively when HDA is present, and $m/z = 141$ and 211 both appear more abundant in the presence of HDA. A straightforward candidate for the identity of the $m/z = 239$ peak is a fragment of α -acyloxyalkyl hydroperoxide esters (AAHPs)

formed from the reaction between either the C₉ or the C₁₄ sCI and HDA, resulting in a C₂₅ or C₃₀ AAHP, respectively (Figure 1A).

Assuming these AAHP products are produced *via* the O-H insertion mechanism,^{28,40} the C-O bond from the carboxylic acid head group of the HDA will be retained as the ester C-O bond in the AAHP product. Upon photoionization, these HDA-derived AAHPs can undergo fragmentation along the C-O bond of the ester group, yielding an [HDA-OH]⁺ fragment at $m/z = 239$, as illustrated in Scheme S1 (*Supporting Information*). Alternately, if photolytic cleavage proceeds along the C-C bond on the opposite side of the carbonyl, the result will be an [HDA-HO₂]⁺ fragment at $m/z = 211$. Since both ions involve the HDA moiety, these peaks should probe the kinetics of both HDA-derived AAHPs in aggregate. As such, only the observed kinetics of $m/z = 239$ are shown in Figure 8.

By similar analysis, $m/z = 141$ can be assigned to a fragment of the AAHP formed from the reaction of either sCI with nonanoic acid, itself the isomerization product of the C₉ sCI (Figure 1A). As for HDA-derived AAHPs, fragmentation of a nonanoic acid-derived AAHP could occur along the ester C-O bond, yielding the observed fragment with $m/z = 141$, or along the alkyl-carbonyl C-C bond, yielding a fragment at $m/z = 113$ (Scheme S2, *Supporting Information*). Although a small peak is observed at $m/z = 113$ in Figure 6, its intensity lies too close to the detection limit to be quantified reliably. The kinetics of the $m/z = 141$ peak, along with corresponding predictions of the nonanoic-derived AAHP kinetics, are shown in Figure S7 (*Supporting Information*).

For tetradecanoic acid-derived AAHPs, C-O cleavage yields a fragment with $m/z = 211$, (Scheme S3, *Supporting Information*) isobaric with the C-C cleavage fragment for the HDA-derived AAHPs, explaining why $m/z = 211$ is visible in the pure Tri spectra in Figure 6. Therefore,

the kinetics of $m/z = 211$ in the presence of HDA, shown in Figure S6 (*Supporting Information*), likely includes contributions from fragments of the tetradecanoic-derived AAHPs. C-C cleavage of the same AAHPs should yield a fragment at $m/z = 183$, where a peak is visible in Figure 6 but of too little intensity to be reliably quantified. The relatively low intensities of the C-C cleavage fragments in both Scheme S2 and S3 are consistent with the ester C-O bond in these species likely being more labile to dissociative photoionization.

Simulation Results

The kinetics of $m/z = 239$ in Figure 8 largely agree with predictions of the total HDA-derived AAHP kinetics from simulations, which depend on a chosen temperature-dependent description of k_{AAHP} . There is no clear temperature-dependence to the growth kinetics of the AAHP products, which provides further evidence that the branching ratio between unimolecular and bimolecular sCI reactions does not change significantly over this temperature range, as examined in detail in the Discussion.

It should be noted that the peak assignments made here are not definitive, and it is conceivable that some of the peaks in Figure 6 could belong to fragments of other reaction products not considered in the mechanism in Figure 1A, such as secondary ozonides (SOZs), which are not observed directly in this study. However, given the symmetric structure of 5-membered SOZ rings, it seems reasonable to expect a nearly even distribution of heavier and lighter fragments from SOZs, which is inconsistent with the observed preference for $m/z = 141$ and 211 fragments over $m/z = 113$ and 183. Nonetheless, sensitivity tests of SOZ formation reactions in the kinetic model have been conducted, and the results are summarized in the *Supporting Information* (Figure S4).

Discussion

Contributions of Various Reactive Sinks to γ_{eff}

As illustrated in Figure 1A, while consumption of Tri is initiated by ozonolysis, Tri can also be consumed by three classes of radical reactions: i) abstraction of a hydrogen atom by an OH radical, ii) OH radical addition to the alkene functionality, and iii) abstraction of a hydrogen atom by an alkoxy (RO) radical. A representation of the individual contributions of all four reactive sinks (ozonolysis and the three radical sinks) to the simulated decay kinetics of Tri, at a fixed ozone exposure of 1×10^{15} molec. $\text{cm}^{-3} \text{sec}^{-1}$, are displayed in the bar chart in Figure 9. Each bar corresponds to one experimental condition (*i.e.*, T , X_{Tri}) represented in Figure 3, with temperature indicated by grouping along the X-axis, and initial X_{Tri} indicated by hatching on the bars. The total height of the bar is proportional to the amount of Tri consumed at the specified ozone exposure, and is proportional to the γ_{eff} predicted by the model. The experimentally-derived γ_{eff} have been overlaid for ease of comparison.

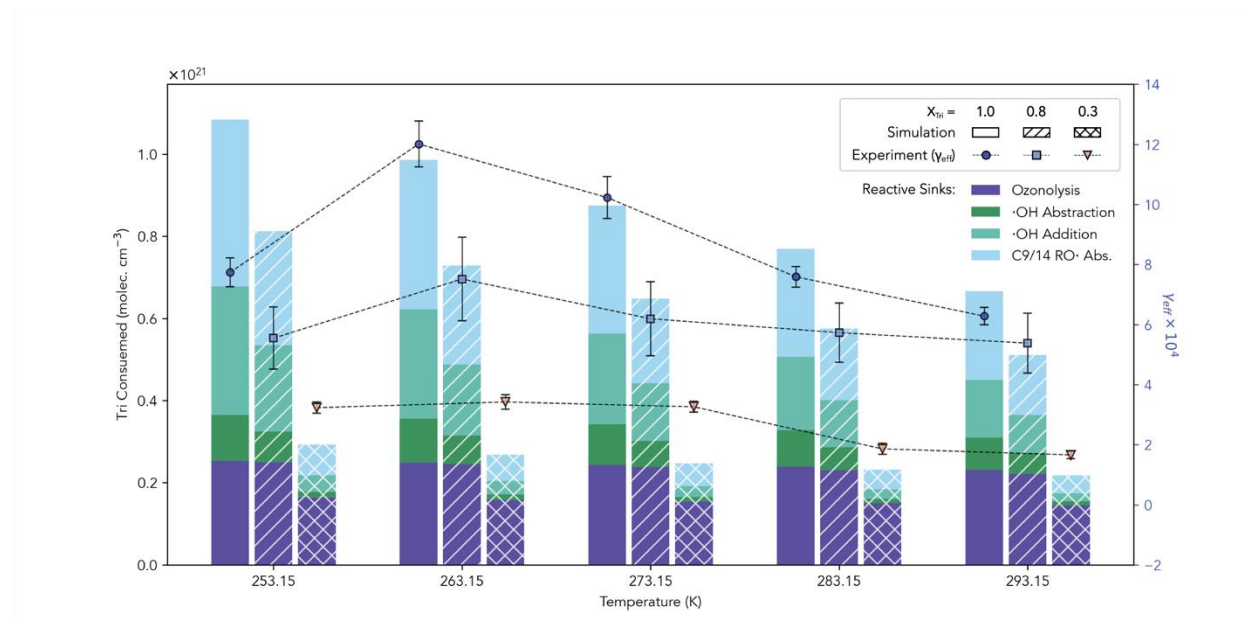


Figure 9. Bar chart displaying the breakdown of the contribution of each Tri sink (in ascending order from the bottom of the bar: ozonolysis, OH abstraction, OH addition, and RO radical abstraction) in the model to the overall consumption of Tri at a fixed ozone exposure of 1×10^{15}

molec. cm⁻³ sec⁻¹. Uptake coefficients from experiments are overlaid (right vertical axis) for comparison.

In the case of pure Tri (unhatched bars), it should be noted that ozonolysis only accounts for approximately a third of the reactivity, with radical reactions accounting for the majority of Tri consumed across all temperatures. This result is consistent with the single-compartment model published previously by Zeng and Wilson for room-temperature (298 K) ozonolysis of Tri aerosol.³² As the initial concentration of HDA is increased at each temperature, the contribution of these radical sinks decreases dramatically, while the contribution of the ozonolysis sink changes very little. Since they are the most sensitive to changes in the chemical environment, the contributions of radical reactions to the Tri decay kinetics are key to unraveling the temperature dependent trend in γ_{eff} reported in this work. As shown in Figure 1A, all radical species responsible for consuming Tri in the model are generated by the unimolecular decomposition channel of the sCI, which creates both OH and RO radicals. Thus, to investigate how the contributions of radical sinks for Tri change with temperature, we must investigate the temperature-dependent kinetics of the sCI, first in pure Tri aerosols and then in the presence of added HDA.

The sCI Population Enhances the Initiation Rate of Radical Reactions

To begin, we revisit the rate law for the sCI formulated in prior work:²⁹

$$\frac{d[\text{sCI}]}{dt} = k_{\text{O}_3}[\text{Tri}][\text{O}_3]_b - [\text{sCI}](k_{\text{iso}} + k_{\text{VHP}} + k_{\text{AAHP}}[\text{HDA}]) \quad (3)$$

By relabeling the production rate of the sCI (the first term of the R.H.S.) as k_1 , the sum of all the sink terms as k_2 , and setting the initial concentration of Tri to be $[\text{Tri}]_0$, the following solution can be found to Equation 3:

$$[sCI](t) = \frac{k_1[Tri]_0}{k_2 - k_1}(e^{-k_1 \cdot t} - e^{-k_2 \cdot t}) \quad (4)$$

To determine the behavior of this expression with variable temperature, it is instructive to look at representative terms for the rates involved in Equation 4. Focusing first on pure Tri aerosols, we assume that $[HDA] = 0$ and the k_{AAHP} term can thus be neglected. The production rate k_1 is therefore proportional to two terms: the ozonolysis reaction rate, which decreases with decreasing temperature, and the bulk concentration of ozone in the particle (approximated by H_{gb}) which increases with decreasing temperature (Figure 1B). The behavior of k_1 is plotted in Figure 10A (blue curve, left vertical axis) and shows a slight increase from 293 to 253 K, indicating that the increased solubility of O_3 is dominant over this temperature range. By contrast, k_{VHP} , the unimolecular decay rate of sCI to yield OH and RO radicals, decreases rapidly over the same temperature range (red curve, right vertical axis). With these functional forms for k_1 and k_2 , the result of equation 4 are plotted against the model predictions of the total sCI population from kinetic simulations in Figure S12 (Supporting Information).

Since all radical chemistry in the model is initiated by unimolecular decay of the sCI, the expected radical contribution to the Tri decay should be proportional to this rate of radical initiation. We may estimate this rate as,

$$k_{VHP}(T) \cdot [sCI]_{tot}(T, X_{Tri}) \quad (5)$$

where $[sCI]_{tot}$ is the time-integrated total amount of sCI produced during reaction at a given temperature, T , and initial mole fraction of Tri, X_{Tri} ,

$$[sCI]_{tot} = \int_0^{\infty} [sCI](t) \cdot dt = \frac{k_1[Tri]_0}{k_2 - k_1} \left(\frac{1}{k_1} - \frac{1}{k_2} \right) \quad (6)$$

The behavior of Equation 6 as a function of temperature is plotted in Figure 10B (dashed black curve). Since both k_1 has a negative temperature dependence and k_2 in pure Tri particles has a

positive temperature dependence, the total sCI formation rate is predicted to increase dramatically at low temperatures. However, due to the rapid fall-off of $k_{\text{VHP}}(T)$ with decreasing temperature, the effective radical initiation rate described in Equation 5 has only a modest negative temperature dependence (green curve, Figure 10B).

Together, these opposing trends—the increasing sCI concentration and decreasing unimolecular decay rate at low temperatures—explain the trend in radical reactivity in Figure 9: although the Tri consumed by ozonolysis remains nearly constant across temperatures, the increased sCI population initiated by ozonolysis drives modest increases in radical chemistry. At low temperatures, these increases contribute significantly to the Tri decay kinetics. This finding highlights the importance of considering secondary reactions when modeling aerosol oxidation at low temperatures. However, it should be noted that this analysis does not include the impact of bimolecular sinks, i.e., the reaction with carboxylic acids, in the sCI sink term k_2 . Therefore, fully understanding the temperature dependent behavior of the sCI population requires a treatment of the sCI branching ratio between bimolecular and unimolecular reactions.

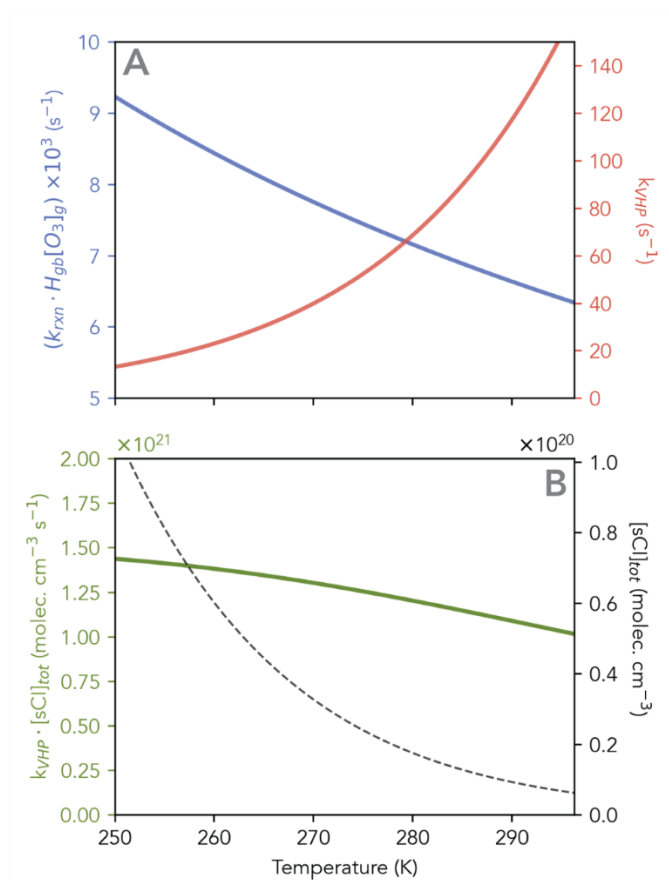


Figure 10. Curves illustrating the temperature-dependent behavior of key parameters in this study. A) the pseudo-first order rate of Tri ozonolysis, corresponding to term k_1 in Equation 4 (blue curve, lefthand vertical axis) and the sCI unimolecular decomposition rate k_{VHP} (red curve, righthand vertical axis). B) The integrated total concentration of sCI produced during reaction with pure Tri aerosols, according to Equation 6 (black dashed curve, righthand vertical axis), and the effective radical initiation reaction rate ($k_{VHP} \cdot [sCI]_{tot}$) during the reaction (green curve, lefthand vertical axis).

The sCI Branching Ratio (k') Balances Unimolecular and Bimolecular Pathways

As seen in Figure 9, when the initial HDA concentration in the particles increases, the reactive contributions of radical reactions decrease significantly. As a result, at high initial HDA concentrations, ozonolysis accounts for a much larger fraction of the Tri consumed during the reaction: for simulations with $X_{Tri}=0.3$ (cross-hatched bars), ozonolysis accounts for roughly two-thirds of the Tri consumption across all temperatures. The decrease in overall Tri consumption

with the addition of HDA is therefore primarily due to the loss of radical reaction sinks *via* the reaction between sCI and HDA.

The kinetics of this reaction can be extrapolated from the decay kinetics of the HDA. In previous work at room temperature, the rate of HDA decay was shown to depend on the ratio of rate constants k' ,²⁹ defined as

$$k' = \frac{k_{AAHP}}{k_{iso} + k_{VHP}} \quad (7)$$

Since other bimolecular sinks were neglected, k' also corresponds to the branching ratio between the bimolecular (numerator of Equation 7) and unimolecular (denominator) sinks of the particle-phase sCI. Fitting to experimental data in that work yielded a k' of $6.59 \pm 0.95 \times 10^{-22} \text{ cm}^3 \text{ molec}^{-1}$ at 293 K, very similar to a value extracted from a modeling study of the ozonolysis of oleic acid particles.⁴¹ Assuming gas-phase literature values for $k_{iso} + k_{VHP}$ at the same temperature, this corresponds to a k_{AAHP} of $1.85 \pm 0.27 \times 10^{-19} \text{ cm}^3 \text{ molec}^{-1} \text{ s}^{-1}$, which was successfully used to model the reaction kinetics. However, to extend this analysis to temperatures lower than 293 K, temperature-dependent descriptions of the rates in Equation 7 must be adopted. Since experimentally-benchmarked theoretical estimates are available for the temperature-dependence of the two unimolecular rates,²² the description of $k_{AAHP}(T)$ in the particle phase will also determine the temperature dependence of k' for the purposes of this study. Four descriptions of $k_{AAHP}(T)$ are chosen corresponding to the four values of the activation energy (E_a) discussed in the Results and detailed in Table S2 and Figure S10 (Supporting Information).

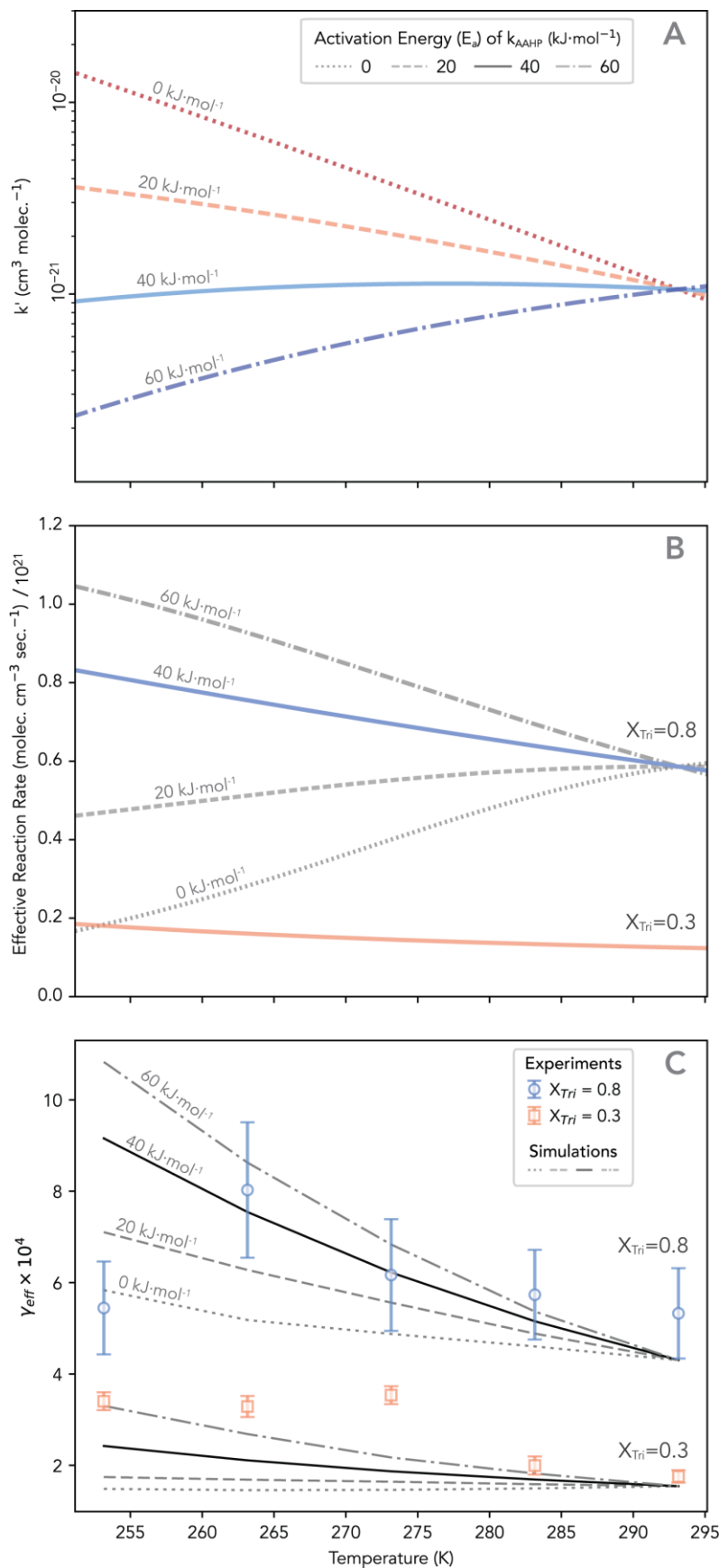


Figure 11. The impacts of the temperature-dependent branching ratio $k'(T)$, between unimolecular and bimolecular reactions involving the sCI, on the overall reaction kinetics. Different possible values for the activation energy (E_a) of k_{AAHP} , as outlined in Table S2, are indicated by line style. A) Plot of k' (Equation 7) on a logarithmic scale as a function of temperature. B) The effective radical initiation reaction rate ($k_{VHP} \cdot [sCI]_{tot}$) during the reaction, including the effects of the k_{AAHP} sink at various values of E_a . C) Effect of changing the k_{AAHP} activation energy (and therefore $k'(T)$) on the simulation-predicted Tri uptake (γ_{eff}) when HDA is present, with experimental γ_{eff} overlaid (points).

Figure 11A shows the computed $k'(T)$ for each choice of E_a for $k_{AAHP}(T)$, as described in the Results. Note that the values of $k_{AAHP}(T)$, and therefore $k'(T)$, all converge at 293 K by construction in order to agree with room temperature measurements. When $E_a=0$, k_{AAHP} is constant across all temperatures, while the unimolecular decay rates falls off at low temperatures. This makes the bimolecular channel increasingly favorable at low temperatures, and thus increasing k' . As E_a is increased, the slope of k' with temperature gradually becomes more positive, reaching a nearly flat slope when $E_a=40 \text{ kJ mol}^{-1}$ (solid line), indicating that the changes in the unimolecular rates and k_{AAHP} under this condition are approximately equal over this temperature range. Thus, an unchanged branching ratio k' with temperature would imply an activation energy of k_{AAHP} on the order of 40 kJ mol^{-1} .

As before for neat Tri aerosols, we may estimate the temperature-dependent population of the sCI produced during the reaction by including the description of $k_{AAHP}(T)$ in the loss term (k_2) in Equation 6. The simulation results and predictions for the sCI population (both assuming an E_a of 40 kJ mol^{-1}) when HDA is present in the aerosol are shown in Figure S12 (Panels B and C, Supporting Information). While lower temperatures still lead to enhanced buildup of sCI during the reaction, the presence of HDA reduces the overall sCI population across the modeled temperature range. Computing the effective radical initiation rate for an initial $X_{Tri}=0.8$ results in the curves plotted in Figure 11B, where the relationship between E_a and the slope of the curves is

opposite the trend in $k'(T)$: as E_a is increased, the reaction with HDA is diminished at low temperatures, causing the sCI to favor unimolecular reactions. Conversely, a smaller E_a results in a diminishing radical initiation rate with decreasing temperature, as reaction with HDA begins to dominate the unimolecular decay rate. It should also be noted that, as expected, the effect of the sCI + acid reaction scales with the initial HDA concentration in the aerosol, leading to the dramatic decrease in the radical initiation rate when X_{HDA} is increased to 0.7 ($X_{\text{Tri}}=0.3$, solid red line).

Thus, the temperature-dependent branching ratio $k'(T)$, and by extension the activation energy of the primary bimolecular sink, controls a significant portion of the reactivity in mixed Tri/HDA aerosols. This effect is evident in the simulated Tri decay kinetics, as shown in Figure 11C. The choice of E_a , and thus the temperature dependence of $k'(T)$, modulates the slope of the uptake coefficient with temperature: smaller values of E_a lead to smaller changes in γ_{eff} with temperature, according to the trend in the radical initiation rate seen in Figure 11B. Comparison between the experimental and simulated γ_{eff} additionally provides evidence of an activation barrier to the reaction between sCI and HDA on the order of 40–60 kJ mol⁻¹, in agreement with modeling of the HDA decay kinetics in Figure 5. However, it should be noted that simulations with no activation barrier still have a slight negative temperature dependence, due to increases in ozone solubility.

Therefore, consistent with the results presented in Figure 9, the net effect of adding HDA to the aerosol mixture is to decrease the effective rate of radical reaction initiation at all temperatures. However, the magnitude of the increase in γ_{eff} requires that the branching ratio $k'(T)$ be sufficiently constant across the temperature range studied here to allow unimolecular reactions to remain competitive. Such a “flat” temperature-dependence of the branching ratio requires a significant activation energy barrier on k_{AAHP} in the particle phase. This result is again

in contrast with gas-phase measurements of the sCI + carboxylic acid reaction, which have been shown to be barrierless and enhanced by long-range interactions between the reactants.^{27,28,40} In particular, Vereecken notes that reactant orientation is crucial in this reaction, as the insertion reaction mechanism implicated in AAHP formation requires the sCI and the acid functional group to adopt a co-planar geometry, likely making this reaction subject to substantial steric effects in the particle phase, which could create an activation barrier. Thus, while the presence of particle-phase acids as bimolecular reaction partners does lead to sCI scavenging at low temperatures, relatively high concentrations of acids (*i.e.*, in excess of the alkene) still appear to be required to shut off the effects of sCI-initiated radical chain cycling.

Conclusion

Together, the experimental data and modeling results presented here highlight how the kinetics of heterogeneous ozonolysis reactions on aerosol particles are strongly determined by the reactivity of particle-phase intermediates, especially unimolecular reactions of the sCI, even at low temperatures. While decreases in temperature lead to decreases in the radical-initiating unimolecular decay rates of sCI, low temperatures also increase the solubility of ozone, leading to increased buildup of reactive intermediate concentrations over the temperature range studied here. Thus, decreases in temperature can have the net effect of enhancing reactivity by indirectly driving increases in secondary chemistry. Additionally, in the presence of a sCI scavenger, such as the saturated acid used here, the activation energy required for the sCI + carboxylic acid reaction in the particle phase leads to decreases in the rate that closely match the decreases in unimolecular rates, maintaining a nearly constant branching ratio between these reactions over the temperature range studied here. This finding would again suggest that, up to a factor of the concentration of

scavenger molecules in the particle phase, unimolecular reactions of particle-phase sCI can remain competitive at low temperatures and continue to drive radical chain chemistry.

These results could have implications for other model systems for heterogeneous reactivity, such as oleic acid, where the importance of secondary chemistry to the overall reactivity has been explored.^{8,41} In particular, an unchanging temperature-dependent branching ratio between bimolecular and unimolecular reactions could explain why the temperature dependence of the uptake of ozone by supercooled oleic acid aerosols appears to be flat.⁷ Due to the high concentration of acid functional groups in oleic acid, bimolecular reactions could modulate both the concentration of particle-phase sCI as well as the radical initiation rate, keeping chain-propagating and chain-terminating reactions in equilibrium before the onset of particle freezing. Future studies could be conducted to explore how well this effect generalizes to similar reaction systems, and to determine the temperature range and conditions over which it is relevant before particle phase effects become dominant.

Finally, avenues for future experimental work include more explicit treatment of particle phase and morphology, both of which affect reactant transport. Experiments with different particle-phase reactants, varied relative humidity, or which include nucleation seeds to induce particle freezing⁴² could help to disentangle the effects of particle morphology from the temperature-dependent chemistry explored here. In addition, the role of the surface in facilitating the reaction with respect to changes in temperature and particle composition is a key question, which could be addressed by size-dependent measurements at low temperatures, which report the scaling of the reactivity with particle surface area, or by surface-sensitive spectroscopic techniques, such as X-ray photoelectron spectroscopy, which could report on the evolving composition of the particle surface during reaction.

Supporting Information: Schematics of the experimental setup and instrumentation (Figures S1–S2), table of reaction rate constants (Table S1) and discussion of parameters used in reaction-diffusion simulations, sensitivity tests of parameters (Figures S3–S4), kinetics of additional peaks identified in main text (Figures S5–S9), proposed ion fragmentation mechanisms (Schemes S1–S3), evaluations of Arrhenius parameters for k_{AAHP} (Table S2, Figures S10–S11), and predicted kinetics of $[sCI]_{tot}$ (Figure S12).

Acknowledgements: This work was supported by the Gas Phase Chemical Physics Program (GPCP), in the Chemical Sciences Geosciences and Biosciences Division of the Office of Basic Energy Sciences of the U.S. Department of Energy under Contract No. DE-AC02-05CH11231.

References:

- (1) Finlayson-Pitts, B. J.; Pitts, J. N. *Chemistry of the Upper and Lower Atmosphere: Theory, Experiments, and Applications*; Academic Press: San Diego, 2000.
- (2) Worsnop, D. R.; Morris, J. W.; Shi, Q.; Davidovits, P.; Kolb, C. E. A Chemical Kinetic Model for Reactive Transformations of Aerosol Particles: REACTIVE TRANSFORMATION OF AEROSOL PARTICLES. *Geophys. Res. Lett.* **2002**, 29 (20), 571–574. <https://doi.org/10.1029/2002GL015542>.
- (3) Wilson, K. R.; Prophet, A. M.; Willis, M. D. A Kinetic Model for Predicting Trace Gas Uptake and Reaction. *J. Phys. Chem. A* **2022**, 126 (40), 7291–7308. <https://doi.org/10.1021/acs.jpca.2c03559>.
- (4) Davies, J. F.; Wilson, K. R. Nanoscale Interfacial Gradients Formed by the Reactive Uptake of OH Radicals onto Viscous Aerosol Surfaces. *Chem. Sci.* **2015**, 6 (12), 7020–7027. <https://doi.org/10.1039/C5SC02326B>.
- (5) Reid, J. P.; Bertram, A. K.; Topping, D. O.; Laskin, A.; Martin, S. T.; Petters, M. D.; Pope, F. D.; Rovelli, G. The Viscosity of Atmospherically Relevant Organic Particles. *Nature Communications* **2018**, 9 (1), 1–14. <https://doi.org/10.1038/s41467-018-03027-z>.
- (6) Slade, J. H.; Ault, A. P.; Bui, A. T.; Ditto, J. C.; Lei, Z.; Bondy, A. L.; Olson, N. E.; Cook, R. D.; Desrochers, S. J.; Harvey, R. M.; Erickson, M. H.; Wallace, H. W.; Alvarez, S. L.; Flynn, J. H.; Boor, B. E.; Petrucci, G. A.; Gentner, D. R.; Griffin, R. J.; Shepson, P. B. Bouncer Particles at Night: Biogenic Secondary Organic Aerosol Chemistry and Sulfate Drive Diel Variations in the Aerosol Phase in a Mixed Forest. *Environ. Sci. Technol.* **2019**, 53 (9), 4977–4987. <https://doi.org/10.1021/acs.est.8b07319>.
- (7) Kaur Kohli, R.; Reynolds, R. S.; Wilson, K. R.; Davies, J. F. Exploring the Influence of Particle Phase in the Ozonolysis of Oleic and Elaidic Acid. *Aerosol Science and Technology* **2024**, 58 (4), 356–373. <https://doi.org/10.1080/02786826.2023.2226183>.

- (8) Berkemeier, T.; Mishra, A.; Mattei, C.; Huisman, A. J.; Krieger, U. K.; Pöschl, U. Ozonolysis of Oleic Acid Aerosol Revisited: Multiphase Chemical Kinetics and Reaction Mechanisms. *ACS Earth Space Chem.* **2021**, *5* (12), 3313–3323. <https://doi.org/10.1021/acsearthspacechem.1c00232>.
- (9) Willis, M. D.; Wilson, K. R. Coupled Interfacial and Bulk Kinetics Govern the Timescales of Multiphase Ozonolysis Reactions. *J. Phys. Chem. A* **2022**, *126* (30), 4991–5010. <https://doi.org/10.1021/acs.jpca.2c03059>.
- (10) Tobias, H. J.; Ziemann, P. J. Thermal Desorption Mass Spectrometric Analysis of Organic Aerosol Formed from Reactions of 1-Tetradecene and O₃ in the Presence of Alcohols and Carboxylic Acids. *Environ. Sci. Technol.* **2000**, *34* (11), 2105–2115. <https://doi.org/10.1021/es9907156>.
- (11) Ziemann, P. J. Aerosol Products, Mechanisms, and Kinetics of Heterogeneous Reactions of Ozone with Oleic Acid in Pure and Mixed Particles. *Faraday Discuss.* **2005**, *130* (0), 469–490. <https://doi.org/10.1039/B417502F>.
- (12) Wang, M.; Yao, L.; Zheng, J.; Wang, X.; Chen, J.; Yang, X.; Worsnop, D. R.; Donahue, N. M.; Wang, L. Reactions of Atmospheric Particulate Stabilized Criegee Intermediates Lead to High-Molecular-Weight Aerosol Components. *Environ. Sci. Technol.* **2016**, *50* (11), 5702–5710. <https://doi.org/10.1021/acs.est.6b02114>.
- (13) Heine, N.; Houle, F. A.; Wilson, K. R. Connecting the Elementary Reaction Pathways of Criegee Intermediates to the Chemical Erosion of Squalene Interfaces during Ozonolysis. *Environ. Sci. Technol.* **2017**, *51* (23), 13740–13748. <https://doi.org/10.1021/acs.est.7b04197>.
- (14) Li, J.; Forrester, S. M.; Knopf, D. A. Heterogeneous Oxidation of Amorphous Organic Aerosol Surrogates by O₃, NO₃, and OH at Typical Tropospheric Temperatures. *Atmospheric Chemistry and Physics* **2020**, *20* (10), 6055–6080. <https://doi.org/10.5194/acp-20-6055-2020>.
- (15) Liu, W.; He, L.; Liu, Y.; Liao, K.; Chen, Q.; Kuwata, M. Suppressed Atmospheric Chemical Aging of Cooking Organic Aerosol Particles in Wintertime Conditions. *Atmos. Chem. Phys.* **2024**, *24* (9), 5625–5636. <https://doi.org/10.5194/acp-24-5625-2024>.
- (16) Moschos, V.; Dzepina, K.; Bhattu, D.; Lamkaddam, H.; Casotto, R.; Daellenbach, K. R.; Canonaco, F.; Rai, P.; Aas, W.; Becagli, S.; Calzolari, G.; Eleftheriadis, K.; Moffett, C. E.; Schnelle-Kreis, J.; Severi, M.; Sharma, S.; Skov, H.; Vestenius, M.; Zhang, W.; Hakola, H.; Hellén, H.; Huang, L.; Jaffrezo, J.-L.; Massling, A.; Nøjgaard, J. K.; Petäjä, T.; Popovicheva, O.; Sheesley, R. J.; Traversi, R.; Yttri, K. E.; Schmale, J.; Prévôt, A. S. H.; Baltensperger, U.; El Haddad, I. Equal Abundance of Summertime Natural and Wintertime Anthropogenic Arctic Organic Aerosols. *Nat. Geosci.* **2022**, *15* (3), 196–202. <https://doi.org/10.1038/s41561-021-00891-1>.
- (17) Su, B.; Zhang, G.; Song, C.; Liang, Y.; Wang, L.; Li, L.; Zhou, Z.; Yan, J.; Wang, X.; Bi, X. Submicron Organic Aerosol Types in the Summertime Arctic: Mixing State, Geographic Distribution, and Drivers. *JGR Atmospheres* **2024**, *129* (17), e2024JD041061. <https://doi.org/10.1029/2024JD041061>.
- (18) Razumovskii, S. D.; Zaikov, G. E. The Solubility of Ozone in Various Solvents. *Russ Chem Bull* **1971**, *20* (4), 616–620. <https://doi.org/10.1007/BF00853885>.
- (19) Biń, A. K. Ozone Solubility in Liquids. *Ozone: Science & Engineering* **2006**, *28* (2), 67–75. <https://doi.org/10.1080/01919510600558635>.

- (20) Panich, N. M.; Ershov, B. G. Solubility of Ozone in Organic Solvents. *Russ J Gen Chem* **2019**, *89* (2), 185–189. <https://doi.org/10.1134/S1070363219020026>.
- (21) Atkinson, R.; Baulch, D. L.; Cox, R. A.; Crowley, J. N.; Hampson, R. F.; Hynes, R. G.; Jenkin, M. E.; Rossi, M. J.; Troe, J.; IUPAC Subcommittee. Evaluated Kinetic and Photochemical Data for Atmospheric Chemistry: Volume II – Gas Phase Reactions of Organic Species. *Atmos. Chem. Phys.* **2006**, *6* (11), 3625–4055. <https://doi.org/10.5194/acp-6-3625-2006>.
- (22) Vereecken, L.; Novelli, A.; Taraborrelli, D. Unimolecular Decay Strongly Limits the Atmospheric Impact of Criegee Intermediates. *Phys. Chem. Chem. Phys.* **2017**, *19* (47), 31599–31612. <https://doi.org/10.1039/C7CP05541B>.
- (23) Lester, M. I.; Klippenstein, S. J. Unimolecular Decay of Criegee Intermediates to OH Radical Products: Prompt and Thermal Decay Processes. *Acc. Chem. Res.* **2018**, *51* (4), 978–985. <https://doi.org/10.1021/acs.accounts.8b00077>.
- (24) Long, B.; Bao, J. L.; Truhlar, D. G. Rapid Unimolecular Reaction of Stabilized Criegee Intermediates and Implications for Atmospheric Chemistry. *Nat Commun* **2019**, *10* (1), 2003. <https://doi.org/10.1038/s41467-019-09948-7>.
- (25) Vereecken, L.; Novelli, A.; Kiendler-Scharr, A.; Wahner, A. Unimolecular and Water Reactions of Oxygenated and Unsaturated Criegee Intermediates under Atmospheric Conditions. *Physical Chemistry Chemical Physics* **2022**, *24* (11), 6428–6443. <https://doi.org/10.1039/D1CP05877K>.
- (26) Krüger, M.; Mishra, A.; Spichtinger, P.; Pöschl, U.; Berkemeier, T. A Numerical Compass for Experiment Design in Chemical Kinetics and Molecular Property Estimation. *J Cheminform* **2024**, *16* (1), 34. <https://doi.org/10.1186/s13321-024-00825-0>.
- (27) Welz, O.; Eskola, A. J.; Sheps, L.; Rotavera, B.; Savee, J. D.; Scheer, A. M.; Osborn, D. L.; Lowe, D.; Murray Booth, A.; Xiao, P.; Anwar H. Khan, M.; Percival, C. J.; Shallcross, D. E.; Taatjes, C. A. Rate Coefficients of C1 and C2 Criegee Intermediate Reactions with Formic and Acetic Acid Near the Collision Limit: Direct Kinetics Measurements and Atmospheric Implications. *Angewandte Chemie* **2014**, *126* (18), 4635–4638. <https://doi.org/10.1002/ange.201400964>.
- (28) Vereecken, L. The Reaction of Criegee Intermediates with Acids and Enols. *Phys. Chem. Chem. Phys.* **2017**, *19* (42), 28630–28640. <https://doi.org/10.1039/C7CP05132H>.
- (29) Reynolds, R.; Ahmed, M.; Wilson, K. R. Constraining the Reaction Rate of Criegee Intermediates with Carboxylic Acids during the Multiphase Ozonolysis of Aerosolized Alkenes. *ACS Earth Space Chem.* **2023**. <https://doi.org/10.1021/acsearthspacechem.3c00026>.
- (30) Gloaguen, E.; Mysak, E. R.; Leone, S. R.; Ahmed, M.; Wilson, K. R. Investigating the Chemical Composition of Mixed Organic–Inorganic Particles by “Soft” Vacuum Ultraviolet Photoionization: The Reaction of Ozone with Anthracene on Sodium Chloride Particles. *International Journal of Mass Spectrometry* **2006**, *258* (1–3), 74–85. <https://doi.org/10.1016/j.ijms.2006.07.019>.
- (31) Hinsberg, W. D.; Houle, F. A. Kinetiscope – A Stochastic Kinetics Simulator, 2020. <http://hinsberg.net/kinetiscope>.
- (32) Zeng, M.; Wilson, K. R. Efficient Coupling of Reaction Pathways of Criegee Intermediates and Free Radicals in the Heterogeneous Ozonolysis of Alkenes. *J. Phys. Chem. Lett.* **2020**, *11* (16), 6580–6585. <https://doi.org/10.1021/acs.jpcllett.0c01823>.

- (33) Gibbs, A. Physical Properties of Insect Cuticular Hydrocarbons: Model Mixtures and Lipid Interactions. *Comparative Biochemistry and Physiology Part B: Biochemistry and Molecular Biology* **1995**, *112* (4), 667–672. [https://doi.org/10.1016/0305-0491\(95\)00119-0](https://doi.org/10.1016/0305-0491(95)00119-0).
- (34) Hearn, J. D.; Smith, G. D. Measuring Rates of Reaction in Supercooled Organic Particles with Implications for Atmospheric Aerosol. *Physical Chemistry Chemical Physics* **2005**, *7* (13), 2549–2551. <https://doi.org/10.1039/B506424D>.
- (35) Katrib, Y.; Biskos, G.; Buseck, P. R.; Davidovits, P.; Jayne, J. T.; Mochida, M.; Wise, M. E.; Worsnop, D. R.; Martin, S. T. Ozonolysis of Mixed Oleic-Acid/Stearic-Acid Particles: Reaction Kinetics and Chemical Morphology. *J. Phys. Chem. A* **2005**, *109* (48), 10910–10919. <https://doi.org/10.1021/jp054714d>.
- (36) 2-Hexyldecanoic Acid; SDS No. 464449; Sigma-Aldrich: St. Louis, MO, 2024. <https://www.sigmaaldrich.com/US/en/sds/Aldrich/464449> (accessed 2024-07-31).
- (37) Wells, J. R.; Morrison, G. C.; Coleman, B. K.; Spicer, C.; Dean, S. W. Kinetics and Reaction Products of Ozone and Surface-Bound Squalene. *J. ASTM Int.* **2008**, *5* (7), 101629. <https://doi.org/10.1520/JAI101629>.
- (38) Donahue, N. M.; Drozd, G. T.; Epstein, S. A.; Presto, A. A.; Kroll, J. H. Adventures in Ozoneland: Down the Rabbit-Hole. *Physical Chemistry Chemical Physics* **2011**, *13* (23), 10848–10857. <https://doi.org/10.1039/C0CP02564J>.
- (39) Cremer, D. Theoretical Determination of Molecular Structure and Conformation. 7. Stereoselectivity of the Ozonolysis Reaction. *J. Am. Chem. Soc.* **1981**, *103* (13), 3619–3626. <https://doi.org/10.1021/ja00403a001>.
- (40) Taatjes, C. A. Criegee Intermediates: What Direct Production and Detection Can Teach Us About Reactions of Carbonyl Oxides. *Annu. Rev. Phys. Chem.* **2017**, *68* (1), 183–207. <https://doi.org/10.1146/annurev-physchem-052516-050739>.
- (41) Gallimore, P. J.; Griffiths, P. T.; Pope, F. D.; Reid, J. P.; Kalberer, M. Comprehensive Modeling Study of Ozonolysis of Oleic Acid Aerosol Based on Real-Time, Online Measurements of Aerosol Composition. *Journal of Geophysical Research: Atmospheres* **2017**, *122* (8), 4364–4377. <https://doi.org/10.1002/2016JD026221>.
- (42) Liu, W.; Liao, K.; Chen, Q.; He, L.; Liu, Y.; Kuwata, M. Existence of Crystalline Ammonium Sulfate Nuclei Affects Chemical Reactivity of Oleic Acid Particles Through Heterogeneous Nucleation. *JGR Atmospheres* **2023**, *128* (12), e2023JD038675. <https://doi.org/10.1029/2023JD038675>.